ADVANCED OPTICAL MATERIALS
www.advopticalmat.de

Asymmetric Silicon Dimers Made by Single-Shot Laser-Induced Transfer Demultiplex Light of Different Wavelengths

*Dmitry V. Obydennov, Daniil A. Shilkin, Dmitry N. Gulkin, Evgeny V. Lyubin, Denis M. Zhigunov, Vladimir O. Bessonov, and Andrey A. Fedyanin**

Nanofabrication technologies significantly influence the development of modern optical science. One of such technologies is laser-induced transfer, which allows the creation of single Mie-resonant spherical particles on a wide range of substrates. This study shows that this method can provide asymmetric dimers at the output: a single femtosecond pulse being focused on a silicon-on-insulator wafer results in appearing two nearly spherical particles of different sizes. The resulting dimers are characterized by scanning electron microscopy, elastic light scattering and Raman spectroscopy to gain insight into their structural properties. Back focal plane imaging and variable-color evanescent-wave illumination are then employed to measure the light scattering patterns from isolated dimers. Due to the interference of the excited resonances, the observed patterns are strongly asymmetric in a range of visible wavelengths, which is consistent with theoretical predictions. The results demonstrate the potential of asymmetric silicon dimers made by single-shot laser-induced transfer for color routing at visible light.

Due to the high refractive index and relatively low absorption losses, a significant prevalence in industry and a wide range of available processing techniques, silicon has been one of the most popular materials in modern photonics.[1–3] Submicron silicon particles are able to exhibit high-quality electric and magnetic Mie resonances in the visible[4,5] and near-infrared ranges,[6,7] which can be used in a variety of applications including enhanced harmonic generation,[8,9] ultrafast optical switching,[10,11] directional scattering and emission of light,[12,13] and color-selective excitation of surface electromagnetic waves.[14,15]

D. V. Obydennov, D. A. Shilkin, D. N. Gulkin, E. V. Lyubin, V. O. Bessonov, A. A. Fedyanin
Faculty of Physics
Lomonosov Moscow State University
Moscow 119991, Russia
E-mail: fedyanin@nanolab.phys.msu.ru
D. M. Zhigunov
Center for Engineering Physics
Skolkovo Institute of Science and Technology
Moscow 121205, Russia

The ORCID identification number(s) for the author(s) of this article can be found under https://doi.org/10.1002/adom.202302276

DOI: 10.1002/adom.202302276

Assembling resonant particles into oligomers and arrays results in hybridization of the resonances and interference of the optical response.[16–22] Dimers of silicon particles have been demonstrated to provide electric and magnetic hot spots in the dimer gap,[23] which offer unique opportunities for optical trapping[24] and nanoantenna applications.[25–29] Independently of varying the size of the particles in a dimer, one can manipulate the relative position of the resonances[30] and achieve directional scattering with higher efficiency.[31] Recent studies have also suggested the use of asymmetric silicon dimers to route the scattering direction depending on the wavelength[32,33] or the intensity of incident light.[34]

Many methods have been developed for fabricating optically resonant silicon structures.[35] Spherical-shaped particles can be produced by chemical synthesis including hydrogen silsesquioxane disproportionation methods,[36–40] plasma synthesis,[41,42] grinding,[43] or laser ablation.[4,44] These methods result in relatively high yields, although do not typically provide control over particle ordering and may require non-trivial post-fabrication processing.[21,45,46] Lithographic techniques[13,47–49] offer a certain freedom in choosing the shape of the produced particles and provide a desired arrangement in two dimensions; however, these methods do not typically allow the creation of spherical particles and more complex 3D structures and have restrictions on the choice of substrate on which structures can be made.

Recently, laser-induced transfer techniques[50–53] have been successfully applied to fabricate near-spherical silicon particles with controllable size and to arrange them in desired patterns.[18,54,55] In these methods, a single femtosecond laser pulse focused on a donor substrate causes the material to melt and form a droplet with momentum directed away from the substrate. The droplet then detaches, falls onto another substrate, and solidifies. Depending on the direction of particle transfer relative to the direction of the laser beam propagation, laser-induced backward and forward transfer techniques are distinguished. When fabricating silicon particles, bulk crystalline silicon,[56] a silicon-on-insulator wafer,[15,18,54] or an amorphous silicon film[55,57,58] can be used as a donor. Depending on the donor substrate and the laser beam parameters, the range of opti-

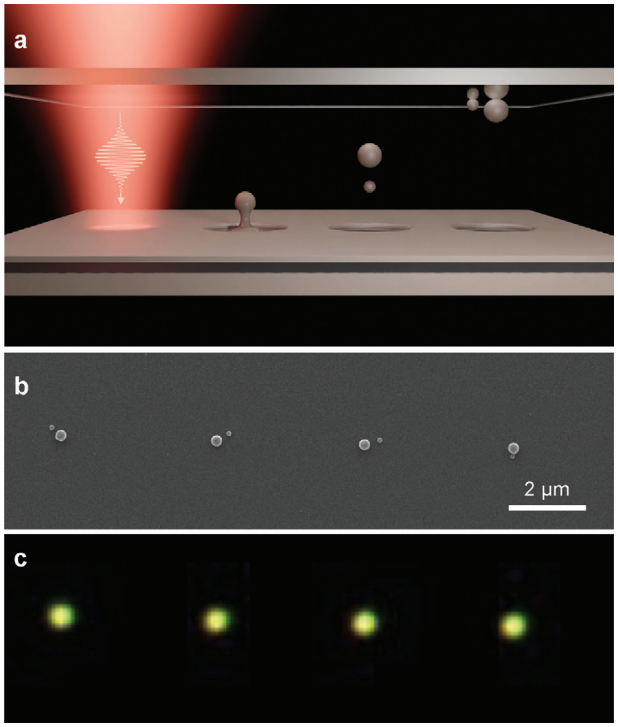

Figure 1. Fabrication of asymmetric silicon dimers by single-shot laser-induced backward transfer. a) Scheme of the fabrication process: a single femtosecond pulse being focused on a SOI wafer results in appearing two spherical particles of different sizes. b) Scanning electron and c) dark-field optical micrographs of the dimers fabricated at the pulse energy of 16 nJ.

cal power providing the creation of single particles is different. In each case, most efforts aim to achieve the conditions for single-particle transfer, while the regime of creating two silicon particles per single laser shot, to the best of our knowledge, has not yet been addressed.

In this article, we report on the fabrication of asymmetric silicon dimers by single-shot laser-induced backward transfer, characterize the structural properties of the fabricated dimers, and demonstrate their operation for color-routing at visible light.

1. Results and Discussion

1.1. Fabrication

The fabrication process is schematically shown in **Figure 1**a. Single pulses from a femtosecond laser source are focused on a silicon-on-insulator (SOI) wafer covered with a thin cover glass. Under the action of laser light, the upper layer of silicon melts, forming droplets of liquid silicon, which then fly onto the glass substrate. The source we used is a commercial laser system (Tsunami femtosecond oscillator and Spitfire regenerative amplifier, Spectra Physics) providing optical pulses with a central wavelength of 800 nm and a nominal pulse duration of 40 fs. The laser beam was passed through a half-wave plate, a Glan prism, and a stack of absorptive neutral density filters to adjust the optical power. The beam was focused on the SOI wafer into a 1.1-μm spot using a 50x Nikon microscope objective lens with a numerical aperture (NA) of 0.45. The SOI wafer had a 50 nm thick upper single-crystalline silicon layer and a 200 nm silicon dioxide layer. The cover glass was 0.15 mm thick and was placed on top of the SOI wafer without a spacer; the distance between the substrates was approximately 5 μm. The relative position of the laser beam waist on the target was controlled by moving the substrates using a motorized translation stage.

Depending on the laser pulse energy, the process results in either no transfer or one, two, or more particles reaching the glass substrate. In our experiments, the smallest single particles were transferred onto the glass substrate at the pulse energy of 14 nJ. When it was raised to 16 nJ, two particles of different sizes were predominantly transferred. With a further increase in pulse energy, the number and size of the transferred particles became less regular. In this study, we will limit the consideration of the fabricated particles to those obtained at the pulse energy of 16 nJ. A scanning electron micrograph of a typical set of such particles is shown in Figure 1b. Here, the distance between neighboring shots was set to 4 μm. In the fabricated dimers, particles have an approximately twofold difference in diameter: 230–240 nm for the bigger and 100–110 nm for the smaller ones. The corresponding dark-field microscopy image of the same set is shown in Figure 1c. The close arrangement of particles in the dimers does not allow distinguishing individual particles under an optical microscope, and each dimer looks like an almost symmetric spot.

In order to characterize single dimers fabricated in our experiments, the transfer procedure was repeated with the distance between neighboring shots set to 10 μm. This allowed us to then collect optical signal from isolated dimers. The prepared arrays also contain single particles, which were obtained when only the bigger droplet reached the glass substrate. Such particles were used for reference measurements.

1.2. Raman Spectroscopy

The laser-induced transfer technique may provide different crystalline states of the fabricated particles. The crystalline state of the particles, in turn, significantly influences their optical response.[54,55] To characterize the particles fabricated in our experiments, we measured their Raman scattering spectra. The measurements were performed using a Horiba LabRam HR Evolution Raman spectrometer attached to a confocal microscope; the excitation was at the wavelength of 532 nm. The beam was focused on the specimen into a spot 4 μm in diameter with an intensity of approximately 0.75 kWcm^{-2}. Both dimers and reference single particles were studied. Among the fabricated dimers, we found one with an exceptionally large distance between particles; for this dimer, we were able to independently collect the Raman scattering from both particles. **Figure 2**a,b shows the spectra obtained for individual particles in this dimer. The peak near 520 cm^{-1} corresponding to the silicon crystalline phase[59] is present in both obtained spectra, as well as in the spectra for all other particles. This peak is slightly asymmetric; it is also red-shifted and broadened compared to that measured for a fully crystalline silicon wafer using the same setup. This fact may indicate the presence of phonon confinement due to the finite size of crystalline silicon grains,[60] intermediate phase of silicon near

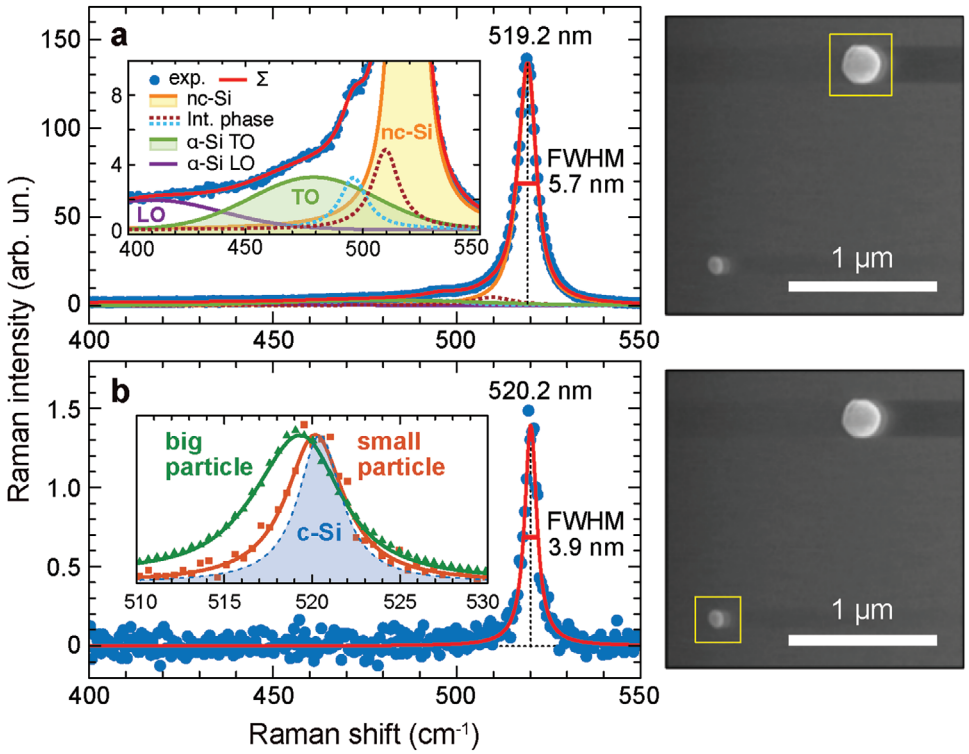

Figure 2. Raman spectroscopy of asymmetric silicon dimers. a,b) Raman scattering spectra of individual particles in the dimer with a large interparticle distance, a) for the big particle and b) for the small one. The measured crystalline peak positions and full widths at half maximum (FWHM) are marked. The inset in (a) shows the enlarged low-frequency wing of the spectrum, and its decomposition into series of modes. Exp. is experimental data, nc-Si is nanocrystalline silicon, α-Si TO, and α-Si LO are modes of amorphous silicon; int. phase is intermediate phase, Σ is the total fitting curve. For the spectrum shown in (b), only nc-Si peak was used for fitting. The inset in (b) shows the peaks of crystalline silicon (blue dashed curve), small particle (orange squares and curve), and big particle (green triangles and curve) normalized by the maximum value for each spectrum. Scanning electron micrographs of the dimer are shown next to the corresponding Raman spectra, with the studied particles marked by yellow squares.

the grain boudaries,[61–64] and inhomogeneous laser heating.[60] Also, significant signal is observed in the region from 300 to 500 cm^{-1} (see the inset in Figure 2a), indicating the presence of the amorphous silicon fraction.[65,66]

To quantify the amount of different fractions, we have decomposed the Raman spectra into series of peaks related to certain vibrational modes. We assumed that the particles contain amorphous and nanocrystalline silicon. Therefore, we considered the longitudinal optical (LO) and transverse optical (TO) modes of amorphous silicon (α-Si), the TO peak of nanocrystalline silicon (nc-Si) according to the phonon confinement model,[67] and two peaks of intermediate phase at the nanocrystal boundaries. The decomposition procedure provided the mean size of silicon nanocrystals d, enabling us to estimate the crystalline volume fraction, or crystallinity, f. For details on the decomposition procedure and extraction of the mentioned parameters, see Section SI (Supporting Information). We have performed this procedure for multiple dimers and single particles. Due to the significant difference in size between the constituent particles in the dimers, the total Raman signal from dimers is determined primarily by the bigger particles; for this reason, we did not distinguish between dimers and big single particles when analyzing the Raman spectra. For the total sample set of 12 dimers and eight single particles, we obtained the mean values of $d = 13.1 \pm 2.5$ nm for the grain size and $f = 0.70 \pm 0.07$ for the crystallinity; see Figure S1 (Supporting Information), for the distributions of the extracted parameters.

When applied to the spectrum shown in Figure 2a, the decomposition procedure resulted in the crystallinity value of $f \simeq 0.70$ for the bigger particle. For the smaller one, the signal-to-noise ratio of the measured Raman intensity was too low to make a reliable prediction on the amorphous silicon fraction. However, one can see in the inset in Figure 2b that the nc-Si peak of the big particle is more red-shifted and broadened than that of the small particle. The peak of the big particle is centered at $\omega_c = 519.2$ cm^{-1} and has a width of $\gamma = 5.7$ cm^{-1}, while the peak of the small particle appears at $\omega_c = 520.2$ cm^{-1} and has a width of $\gamma = 3.9$ cm^{-1}. The corresponding values measured for crystalline silicon at similar conditions are $\omega_c = 520.5$ cm^{-1} and $\gamma = 2.9$ cm^{-1}. Noteworthy, the spectral positions of the c-Si peak and the peak measured for the small particle differ within the spectrometer spectral resolution, which was 0.5 cm^{-1}. In accordance with the phonon confinement model, described in Ref. [67], the mean grain size for the big particle is approximately 12 nm, and for the small particle is at least 30 nm while its diameter is about 110 nm. This difference can be explained by different cooling conditions of the two particles. The dependence of the crystalline state of the laser-transferred silicon particles on the distance between the donor and receiving substrates was previously reported in the literature.[55] From atomistic simulations, it was found that the crystalline grain size

was larger at a smaller cooling rate. In our case, the distance between the substrates is fixed; however, the particles have significant difference in size and may have different speed during the transfer, resulting in different cooling times and cooling rates in air and on the glass substrate. The particle cooling occurs in two stages: cooling in air and cooling on the substrate. The rate of cooling in the air is directly proportional to the particle's surface area and inversely proportional to its volume. Consequently, small droplets undergo cooling approximately twice as fast as big ones. At the same time, smaller particles experience more rapid deceleration than the big ones due to the viscous friction in the air. Therefore, small particles, having a prolonged flight time and faster cooling rate, have a greater chance of crystallizing in air, but the cooling rate is still sufficiently small so that the particle can end up fully crystalline.[55] In contrast, larger particles land on the receiver substrate uncrystallized and undergo an order-of-magnitude faster cooling process upon contact with the glass substrate. This rapid thermal exchange leads to the formation of small crystalline grains, typically measuring around ten nanometers in size.

1.3. Elastic Scattering Spectroscopy

We followed up with dark-field forward scattering spectroscopy of individual dimers to characterize their optical resonances. In these measurements, we used the setup described elsewhere.[68] Scattering spectra of a typical dimer for two orthogonal polarizations of incident light are shown in **Figure 3a**; a scanning electron micrograph of the dimer and orientations of the incident light polarization are shown in the inset. A number of peaks are clearly identified in the spectra, revealing the excitation of low-order Mie resonances in the dimer.

Figure 3b demonstrates the scattering spectra calculated by finite-difference time-domain simulations taking into account the presence of the substrate and the experimental conditions of the collection; see Section SII (Supporting Information), for details of these simulations. The lateral dimensions of both particles in the model were set as determined from the scanning electron micrograph. The smaller particle was considered as a sphere, while the bigger one was considered as a spheroid whose third dimension was set to provide the best fit to the measured spectra. The position and width of the most pronounced scattering peaks in the resulting calculated dependences are in agreement with the experimental data. We additionally ran simulations for each of the constituent particles separately; see Figure S3 (Supporting Information), for the results. The scattering from the smaller particle was found to be at least an order of magnitude lower in intensity than that from the bigger one. The pronounced peaks present in the red and near infrared regions in the scattering from the dimer correspond to the resonances of the bigger particle; however, the presence of the small particle causes dependence on the polarization of the incident light. It can be shown that this dependence is mainly caused by the modification of the electric dipole polarizability due to the near-field interaction (see Section SII, Supporting Information, for multipole decomposition of the scattering spectra of a dimer). Scattering spectra of symmetric silicon dimers have been thoroughly studied in earlier works,[17,18,21] and hybridization of dipolar modes of constituent

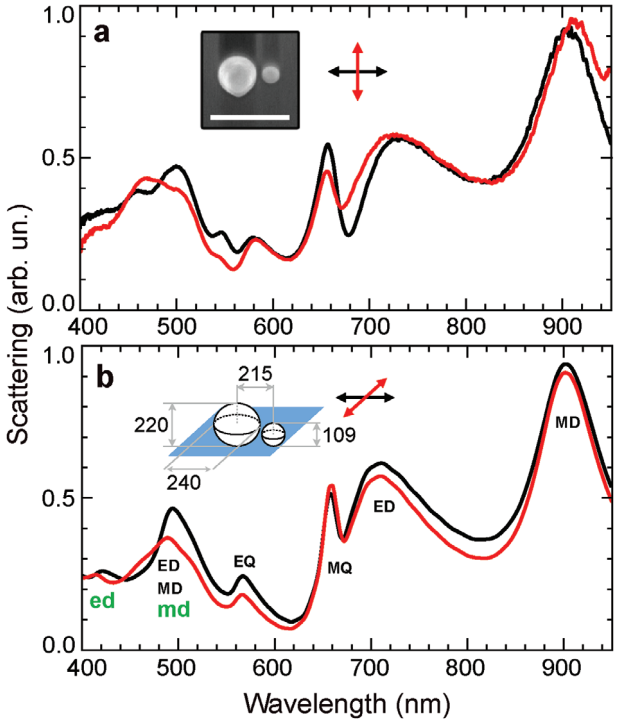

Figure 3. Elastic scattering spectroscopy of asymmetric dimers. a) Experimental scattering spectra of a typical dimer for two linear polarizations of the incident light. The inset shows the scanning electron micrograph and the polarization orientations with respect to the dimer. The scale bar is 500 nm. b) Calculated scattering spectra of a silicon dimer with the geometry shown in the inset; units in nanometers. The main peaks are marked: ed, md — electric and magnetic dipole modes; eq, mq — electric and magnetic qudrupoles; black small capitals are for the big particle, green lowercases are for the small particle.

particles has been theoretically described.[18] In the system under study, as we will show below, hybridization causes only modulation of the scattering intensity and does not significantly affect the scattering directivity.

Other dimer samples were found to have similar scattering spectra, which are also in agreement with the results of numerical calculations, if the configuration of each particular dimer is properly specified in the model. The scattering spectra were also measured for the reference single particles fabricated under the same conditions. For such particles, the influence of the polarization of the incident light on the scattering spectrum was found to be significantly smaller. The results of scattering measurements and numerical simulations for some other dimers and single particles can be found in Section SIII (Supporting Information).

1.4. Back Focal Plane Imaging

Due to the excitation of multiple Mie resonances, the fabricated dimers scatter light in different directions with different efficiencies depending on the wavelength of light. To characterize this dependence experimentally, we studied the directivity of evanescent wave scattering at the fabricated dimers using a home-built back focal plane (BFP) imaging setup; see Section SIV (Supporting In-

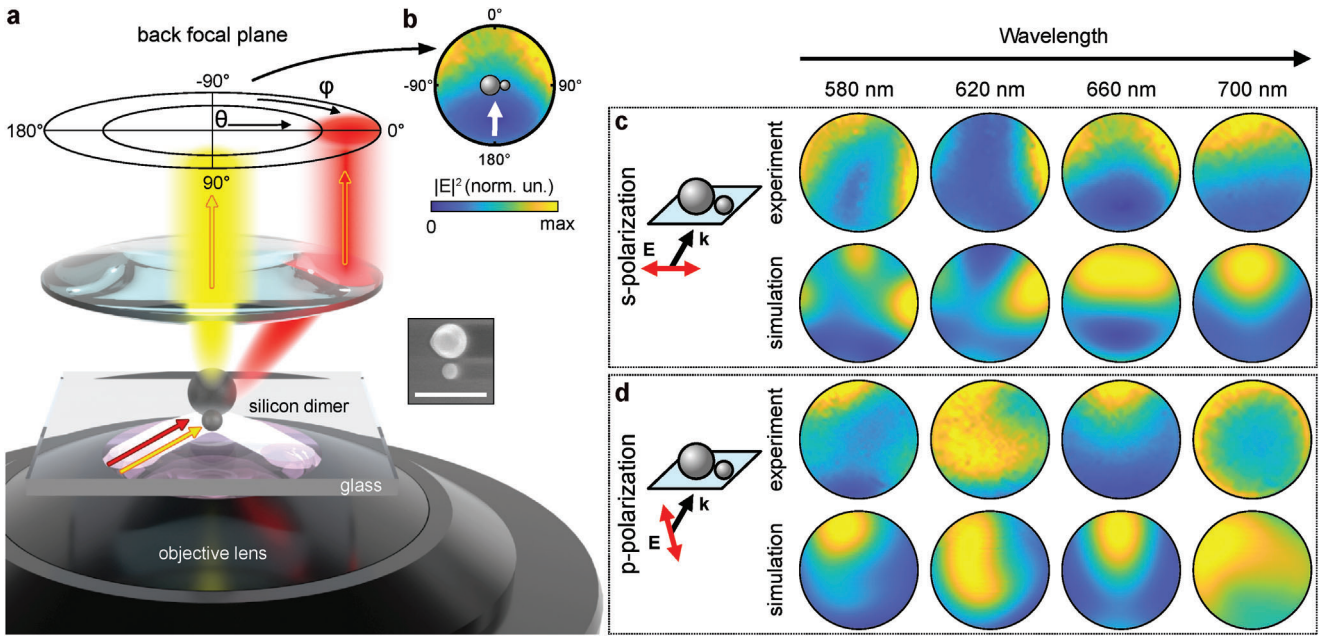

Figure 4. BFP imaging of the evanescent wave scattering at a dimer. a) Scheme of the measurements. Inset: scanning electron micrograph of the studied dimer; the scale bar is 500 nm. b) Example of the back focal plane image showing the orientation of the dimer and the direction of the incident beam (white arrow). c,d) Back focal plane images at different wavelengths for (c) s- and (d) p-polarized incident light. The images are limited to the experimental NA of 0.85, corresponding to the maximal angle of 58°.

formation), for the full description of the setup. A schematic illustration of the experimental configuration is shown in **Figure** 4a. The sample particles were illuminated by an evanescent wave of variable color. For this purpose, spectrally filtered light from a supercontinuum source was directed to the aperture edge of an oil-immersion objective lens designed for total internal reflection fluorescence microscopy. The light scattered by the dimer was collected using a dry objective lens with the NA of 0.85. The direction of the incident evanescent wave was orthogonal to the dimer symmetry axis as shown in Figure 4b. We recorded the images of the BFP of the dry objective at the wavelength varied in the range from 550 to 770 nm for two polarizations of the incident light. Figure 4c,d shows the obtained BFP images for a typical dimer, the scattering spectra and dimensions of which are presented in Figure 3.

The results of numerical simulations also given in Figure 4c,d are in agreement with the experimental data; see Section SV (Supporting Information), for details of the evanescent wave scattering simulations. For large polar angles θ, the asymmetry of scattering is more noticeable in the case of s-polarization and especially pronounced at the wavelength of 620 nm.

The scattering response of particle dimers is generally determined by the interference of scattering from the constituent particles and hybridization of their resonant modes.[18] In our case, since one of the particles is non-resonant in the considered spectral range, the hybridization is not expected to provide a significant effect on the scattering directivity, and the latter can be determined as a result of interference of the far-field response from two closely located non-interacting scatterers. To verify this assumption, we considered a hybridization-free model, in which the scattering contributions from the isolated particles were computed separately and then summed up with a proper phase shift that corresponds to the separation distance between the particles:

$$\mathbf{E}_{\text{dimer}}(\theta,\varphi) = \mathbf{E}_{\text{big}}(\theta,\varphi) + \mathbf{E}_{\text{small}}(\theta,\varphi)\exp\left(-i\frac{2\pi d}{\lambda}\sin\varphi\sin\theta\right) \quad (1)$$

where $\mathbf{E}_{\text{dimer}}$ is the far-field of light scattered by the dimer, $\mathbf{E}_{\text{big}}$ and $\mathbf{E}_{\text{small}}$ are those for the individual big and small particles, correspondingly, λ is the wavelength of light, d is the projection of the distance between the centers of the particles onto the plane of the substrate, θ and φ are the polar and azimuthal angles of the spherical coordinate system (see Figure 4a). **Figure** 5 shows the far-field scattering patterns calculated for individual particles and their sum with the proper phase shift at the wavelength of 620 nm, which corresponds to the most pronounced asymmetry according to the calculations for s-polarized illumination. The hybridization-free model indeed reproduces the scattering asymmetry observed experimentally and in the full–wave numerical simulations (look at Figure 4c for the same wavelength of 620 nm). We also found that s-polarized excitation yields a pronounced overlap of the far field scattering patterns of the two particles in the case of large polar angles θ, facilitating constructive interference in the direction toward the small particle, and destructive interference toward the big particle. For p-polarized illumination, the patterns overlap and interfere at small angles θ.

In the hybridization-free model, one can independently address specific multipoles excited in each of the particles. We performed the multipole decomposition of internal electromagnetic fields calculated for each of the particles, considering the spherical multipole moments up to quadrupoles according to

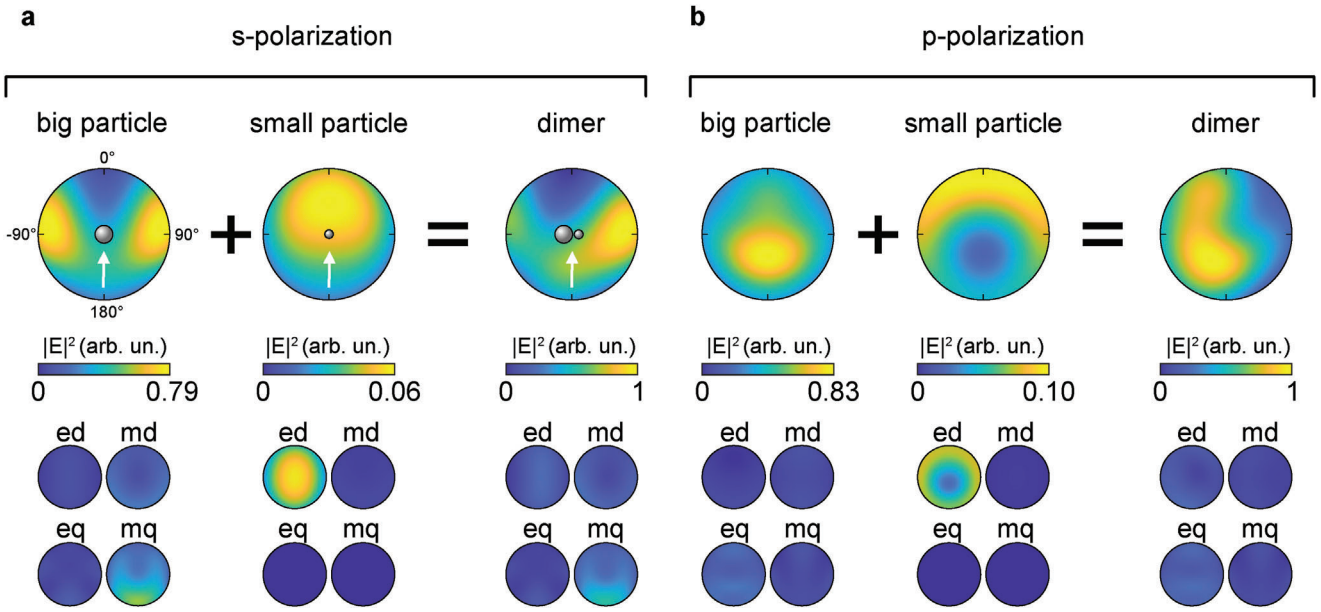

Figure 5. Simulated far-field scattering patterns at the wavelength of 620 nm for individual particles ("big particle", "small particle") and their interference obtained by applying the hybridization-free model ("dimer"), a) s-polarization, b) p-polarization. The contributions from multipole terms into the far-field scattering patterns, including the "ed" (electric dipole),"md" (magnetic dipole), "eq" (electric quadrupole), and "mq" (magnetic quadrupole), are displayed below. The scattering patterns are limited to the experimental NA of 0.85.

Refs. [69–71]. Using the resulting multipole moments, we calculated far-fields. The bottom panel in Figure 5 shows the obtained multipole contributions to the resulting far-field scattering patterns. At the wavelength of 620 nm, the field within the big particle exhibits a complex interplay of all four considered multipoles, while in the small particle, almost exclusively the contribution of the electric dipole is observed. Based on these results, we can characterize the total scattering as resulting from the interference of multiple modes of the big particle with the electric dipole excited in the small particle.

1.5. Analysis of Scattering Directivity

The employed fabrication technique allows depositing asymmetric silicon dimers on a broad range of planar and 3D structures. Due to the wavelength-dependent scattering directivity, these dimers can operate as color demultiplexors in photonic circuits. To demonstrate the color-routing properties of the fabricated dimers, in **Figure 6b** we plot the scattering signal as a function of the wavelength and the azimuthal angle φ. To get this dependence, for each wavelength and angle φ, the scattering intensity was integrated over a circular sector with a central angle of $\Delta\varphi = 20°$ (shown in Figure 6a by green lines). This procedure was performed for both experimental and simulated scattering patterns, and the resulting dependences are in excellent agreement. For s-polarized illumination, light is primarily scattered to the forward direction ($\varphi = 0°$) at the wavelength exceeding 670 nm, and to the right ($\varphi = 90°$) in the spectral range from 610 to 650 nm.

The same analysis performed for experimental results for a reference single particle resulted in a significantly more symmetric dependence in accordance with the numerical simulations. Additional back focal plane measurements for the single particle and another dimer are given in Section SVI (Supporting Information).

Based on the results obtained, we conclude that for the effective separation of light of different wavelengths using the studied dimers, two channels should be used that collect light scattered in the forward and right directions. To quantitatively characterize the color-separation performance of the fabricated dimers, we calculated the directionality figure of merit, as proposed in Ref. [33] for asymmetric disk dimers. We considered the following angle ranges for the "forward" direction: $\varphi = -10° \pm 15°$, $\theta = 50° \pm 10°$, and for the "right" direction: $\varphi = 75° \pm 15°$, $\theta = 50° \pm 10°$. The considered angle ranges are shown in Figure 6a by the red lines and letters "F" and "R", correspondingly. The directionality D was calculated using the following expression:[33]

$$D = 10\log_{10}\frac{I_F}{I_R} \tag{2}$$

where I_F and I_R are integral intensities into the "forward" and "right" directions, correspondingly. The results of the calculations are shown in Figure 6c. In the case of s-polarized excitation, the directionality changes its sign at the wavelength of approximately 650 nm, which corresponds to switching between the right and forward directions of scattering. The modulation from −8 dB at the wavelength of $\lambda = 630$ nm to 3 dB at the wavelength of $\lambda = 700$ nm is observed in the experiment, and from −10 dB for $\lambda = 620$ nm to 5 dB for $\lambda = 700$ nm in the calculations. Light at these wavelengths can be separated using the studied dimers. For this purpose, two waveguides can be used with the facets placed in front and to the right of the dimer. In this case, one can expect

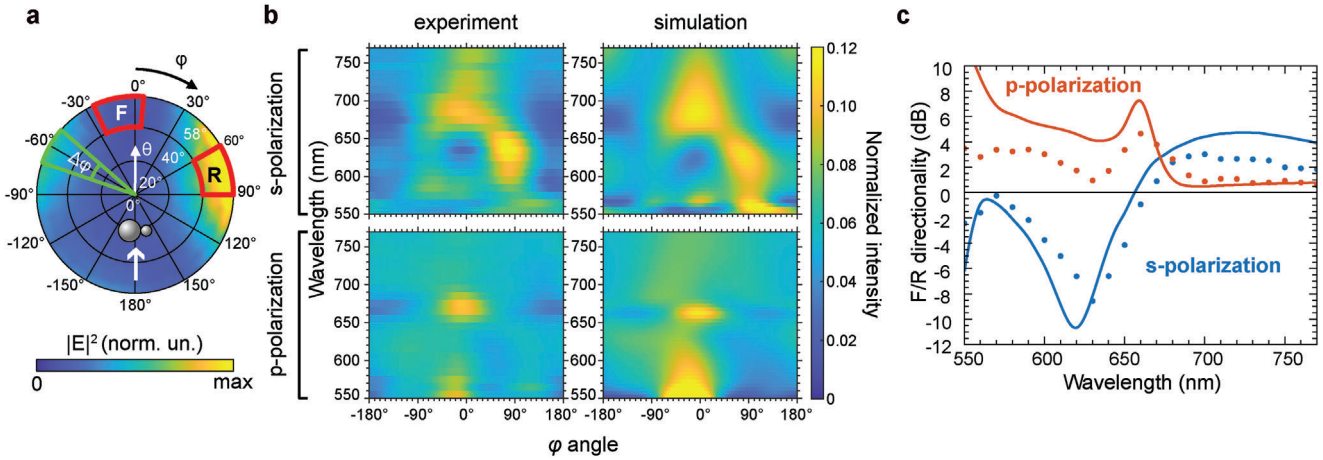

Figure 6. Analysis of scattering directivity. a) Example of the BFP image with the coordinate grid. The red outlines and letters "F" and "R" show the two directions used later for directionality calculations. b) Intensity as a function of the angle φ and wavelength for two polarizations of the incident radiation. For each wavelength and angle φ, the integral intensity in the sector with a central angle $\Delta\varphi = 20°$, normalized to the overall intensity, is shown. An example of the sector for $\varphi = -60°$ is represented in a) by green lines. c) Directionality calculated by Equation (2) for two polarizations of the incident radiation. Dots are experimental values, curves are the result of numerical simulations.

that light of the mentioned wavelengths will be exclusively coupled into the intended waveguide. The modulation is expected to be stronger in the case of shorter wavelengths where the small particle is resonant, and forward scattering with a higher directionality is observed (see Section SVI, Supporting Information, for calculations for shorter wavelengths).

2. Conclusion

We have shown that single-shot laser-induced transfer can provide asymmetric silicon dimers at the output. By using back focal plane imaging and evanescent-wave illumination, we have measured the light scattering patterns from isolated dimers as a function of the wavelength and polarization of incident light. The observed scattering patterns are strongly asymmetric in a range of visible wavelengths. The results of our semi-analytical model reveal that the origin of this asymmetry is the interference of multiple Mie modes of the bigger particle and electric dipole scattering from the smaller one. The results demonstrate the potential of asymmetric silicon dimers made by single-shot laser-induced transfer for color routing at visible light.

3. Experimental Section

Detailed description of the Raman spectra processing, numerical calculations of scattering spectra and far-field scattering patterns, back focal plane imaging setup, and additional scattering spectroscopy and back focal plane imaging results are avaliable in Supporting Information.

Supporting Information

Supporting Information is available from the Wiley Online Library or from the author.

Acknowledgements

The laser-induced transfer experiments were performed by D.A.S. and D.M.Z. in Boris Chichkov's group in 2019. The authors were grateful to Vsevolod Avilkin for assistance in preliminary experiments on BFP imaging. Raman spectroscopy study was performed using the equipment of the "Bioimaging and Spectroscopy" Core Facility of the Skolkovo Institute of Science and Technology. This work was partially supported by the Russian Science Foundation grant 20-12-00371 for scattering spectroscopy and BFP measurements. D.V.O. acknowledged support from the Foundation for the Theoretical Physics and Mathematics Advancement Foundation "BASIS". This research was performed according to the Development program of the Interdisciplinary Scientific and Educational School of the Lomonosov Moscow State University "Photonic and Quantum technologies. Digital medicine".

Conflict of Interest

The authors declare no conflict of interest.

Data Availability Statement

The data that support the findings of this study are available on request from the corresponding author.

Keywords

back focal plane imaging, laser printing, Mie resonances, nanoantenna, silicon photonics, wavelength demultiplexer

Received: September 15, 2023
Revised: November 27, 2023
Published online: December 25, 2023

[1] A. I. Kuznetsov, A. E. Miroshnichenko, M. L. Brongersma, Y. S. Kivshar, B. Luk'yanchuk, *Science* **2016**, *354*, aag2472.

[2] I. Staude, J. Schilling, *Nat. Photon.* **2017**, *11*, 274.
[3] P. Vabishchevich, Y. Kivshar, *Photonics Res.* **2023**, *11*, B50.
[4] A. B. Evlyukhin, S. M. Novikov, U. Zywietz, R. L. Eriksen, C. Reinhardt, S. I. Bozhevolnyi, B. N. Chichkov, *Nano Lett.* **2012**, *12*, 3749.
[5] A. I. Kuznetsov, A. E. Miroshnichenko, Y. H. Fu, J. Zhang, B. Luk'yanchuk, *Sci. Rep.* **2012**, *2*, 492.
[6] E. Xifré-Pérez, R. Fenollosa, F. Meseguer, *Opt. Express* **2011**, *19*, 3455.
[7] L. Shi, T. U. Tuzer, R. Fenollosa, F. Meseguer, *Adv. Mater.* **2012**, *24*, 5934.
[8] M. R. Shcherbakov, D. N. Neshev, B. Hopkins, A. S. Shorokhov, I. Staude, E. V. Melik-Gaykazyan, M. Decker, A. A. Ezhov, A. E. Miroshnichenko, I. Brener, A. A. Fedyanin, Y. S. Kivshar, *Nano Lett.* **2014**, *14*, 6488.
[9] S. V. Makarov, M. I. Petrov, U. Zywietz, V. Milichko, D. Zuev, N. Lopanitsyna, A. Kuksin, I. Mukhin, G. Zograf, E. Ubyivovk, D. A. Smirnova, S. Starikov, B. N. Chichkov, Y. S. Kivshar, *Nano Lett.* **2017**, *17*, 3047.
[10] S. Makarov, S. Kudryashov, I. Mukhin, A. Mozharov, V. Milichko, A. Krasnok, P. Belov, *Nano Lett.* **2015**, *15*, 6187.
[11] M. R. Shcherbakov, P. P. Vabishchevich, A. S. Shorokhov, K. E. Chong, D.-Y. Choi, I. Staude, A. E. Miroshnichenko, D. N. Neshev, A. A. Fedyanin, Y. S. Kivshar, *Nano Lett.* **2015**, *15*, 6985.
[12] Y. H. Fu, A. I. Kuznetsov, A. E. Miroshnichenko, Y. F. Yu, B. Luk'yanchuk, *Nat. Commun.* **2013**, *4*, 1527.
[13] I. Staude, A. E. Miroshnichenko, M. Decker, N. T. Fofang, S. Liu, E. Gonzales, J. Dominguez, T. S. Luk, D. N. Neshev, I. Brener, Y. Kivshar, *ACS Nano* **2013**, *7*, 7824.
[14] I. S. Sinev, A. A. Bogdanov, F. E. Komissarenko, K. S. Frizyuk, M. I. Petrov, I. S. Mukhin, S. V. Makarov, A. K. Samusev, A. V. Lavrinenko, I. V. Iorsh, *Laser Photonics Rev.* **2017**, *11*, 1700168.
[15] D. N. Gulkin, A. A. Popkova, B. I. Afinogenov, D. A. Shilkin, K. Kuršelis, B. N. Chichkov, V. O. Bessonov, A. A. Fedyanin, *Nanophotonics* **2021**, *10*, 2939.
[16] S. Kruk, Y. Kivshar, *ACS Photonics* **2017**, *4*, 2638.
[17] J. Yan, P. Liu, Z. Lin, H. Wang, H. Chen, C. Wang, G. Yang, *ACS Nano* **2015**, *9*, 2968.
[18] U. Zywietz, M. K. Schmidt, A. B. Evlyukhin, C. Reinhardt, J. Aizpurua, B. N. Chichkov, *ACS Photonics* **2015**, *2*, 913.
[19] J. van de Groep, T. Coenen, S. A. Mann, A. Polman, *Optica* **2016**, *3*, 93.
[20] L. Wang, S. Kruk, L. Xu, M. Rahmani, D. Smirnova, A. Solntsev, I. Kravchenko, D. Neshev, Y. Kivshar, *Nanoscale* **2017**, *9*, 2201.
[21] H. Negoro, H. Sugimoto, T. Hinamoto, M. Fujii, *Adv. Opt. Mater.* **2022**, *10*, 2102750.
[22] S. You, M. Zhou, L. Xu, D. Chen, M. Fan, J. Huang, W. Ma, S. Luo, M. Rahmani, C. Zhou, et al., *Nanophotonics* **2023**, *12*, 2051.
[23] R. M. Bakker, D. Permyakov, Y. F. Yu, D. Markovich, R. Paniagua-Domínguez, L. Gonzaga, A. Samusev, Y. Kivshar, B. Luk'yanchuk, A. I. Kuznetsov, *Nano Lett.* **2015**, *15*, 2137.
[24] Z. Xu, W. Song, K. B. Crozier, *ACS Photonics* **2018**, *5*, 4993.
[25] B. Rolly, B. Bebey, S. Bidault, B. Stout, N. Bonod, *Phys. Rev. B* **2012**, *85*, 245432.
[26] P. Albella, M. A. Poyli, M. K. Schmidt, S. A. Maier, F. Moreno, J. J. Sáenz, J. Aizpurua, *J. Phys. Chem. C* **2013**, *117*, 13573.
[27] M. Caldarola, P. Albella, E. Cortés, M. Rahmani, T. Roschuk, G. Grinblat, R. F. Oulton, A. V. Bragas, S. A. Maier, *Nat. Commun.* **2015**, *6*, 7915.
[28] R. Regmi, J. Berthelot, P. M. Winkler, M. Mivelle, J. Proust, F. Bedu, I. Ozerov, T. Begou, J. Lumeau, H. Rigneault, et al., *Nano Lett.* **2016**, *16*, 5143.
[29] M. Humbert, R. Hernandez, N. Mallet, G. Larrieu, V. Larrey, F. Fournel, F. Guérin, E. Palleau, V. Paillard, A. Cuche, L. Ressier, *Nanoscale* **2023**, *15*, 599.
[30] Z.-Y. Jia, J.-N. Li, H.-W. Wu, C. Wang, T.-Y. Chen, R.-W. Peng, M. Wang, *J. Appl. Phys.* **2016**, *119*, 074302.
[31] T. Shibanuma, P. Albella, S. A. Maier, *Nanoscale* **2016**, *8*, 14184.
[32] P. Albella, T. Shibanuma, S. A. Maier, *Sci. Rep.* **2015**, *5*, 18322.
[33] T. Shibanuma, T. Matsui, T. Roschuk, J. Wojcik, P. Mascher, P. Albella, S. A. Maier, *ACS Photonics* **2017**, *4*, 489.
[34] D. G. Baranov, S. V. Makarov, A. E. Krasnok, P. A. Belov, A. Alù, *Laser Photonics Rev.* **2016**, *10*, 1009.
[35] M. L. De Marco, S. Semlali, B. A. Korgel, P. Barois, G. L. Drisko, C. Aymonier, *Angew. Chem. Int. Ed.* **2018**, *57*, 4478.
[36] M. L. De Marco, T. Jiang, J. Fang, S. Lacomme, Y. Zheng, A. Baron, B. A. Korgel, P. Barois, G. L. Drisko, C. Aymonier, *Adv. Funct. Mater.* **2021**, *31*, 2100915.
[37] L. Shi, J. T. Harris, R. Fenollosa, I. Rodriguez, X. Lu, B. A. Korgel, F. Meseguer, *Nat. Commun.* **2013**, *4*, 1904.
[38] A. N. Thiessen, M. Ha, R. W. Hooper, H. Yu, A. O. Oliynyk, J. G. C. Veinot, V. K. Michaelis, *Chem. Mater.* **2019**, *31*, 678.
[39] C. M. Hessel, E. J. Henderson, J. G. C. Veinot, *Chem. Mater.* **2006**, *18*, 6139.
[40] C. M. Hessel, D. Reid, M. G. Panthani, M. R. Rasch, B. W. Goodfellow, J. Wei, H. Fujii, V. Akhavan, B. A. Korgel, *Chem. Mater.* **2012**, *24*, 393.
[41] M. A. Eslamisaray, P. R. Wray, Y. Lee, G. M. Nelson, O. Ilic, H. A. Atwater, U. R. Kortshagen, *Nano Lett.* **2023**, *23*, 1930.
[42] P. R. Wray, M. A. Eslamisaray, G. M. Nelson, O. Ilic, U. R. Kortshagen, H. A. Atwater, *ACS Appl. Mater. Interfaces* **2022**, *14*, 23624.
[43] W. Chaâbani, J. Proust, A. Movsesyan, J. Béal, A. L. Baudrion, P. M. Adam, A. Chehaidar, J. Plain, *ACS Nano* **2019**, *13*, 4199.
[44] C.-Q. Li, C.-Y. Zhang, Z.-S. Huang, X.-F. Li, Q.-F. Dai, S. Lan, S.-L. Tie, *J. Phys. Chem. C* **2013**, *117*, 24625.
[45] D. A. Shilkin, E. V. Lyubin, M. R. Shcherbakov, M. Lapine, A. A. Fedyanin, *ACS Photonics* **2017**, *4*, 2312.
[46] C. Zaza, I. L. Violi, J. Gargiulo, G. Chiarelli, L. Schumacher, J. Jakobi, J. Olmos-Trigo, E. Cortes, M. König, S. Barcikowski, et al., *ACS Photonics* **2019**, *6*, 815.
[47] P. Spinelli, M. Verschuuren, A. Polman, *Nat. Commun.* **2012**, *3*, 692.
[48] M. I. Shalaev, J. Sun, A. Tsukernik, A. Pandey, K. Nikolskiy, N. M. Litchinitser, *Nano Lett.* **2015**, *15*, 6261.
[49] X. Cao, Y. Xiao, Q. Dong, S. Zhang, J. Wang, L. Wang, L. Gao, *Adv. Photonics Res.* **2022**, *3*, 2200127.
[50] A. I. Kuznetsov, J. Koch, B. N. Chichkov, *Opt. Express* **2009**, *17*, 18820.
[51] A. I. Kuznetsov, C. Unger, J. Koch, B. N. Chichkov, *Appl. Phys. A* **2012**, *106*, 479.
[52] V. Valuckas, R. Paniagua-Domínguez, A. Maimaiti, P. P. Patra, S. K. Wong, R. Verre, M. Käll, A. I. Kuznetsov, *ACS Photonics* **2019**, *6*, 2141.
[53] Z. U. Rehman, F. Yang, M. Wang, T. Zhu, *Opt. Laser Technol.* **2023**, *160*, 109065.
[54] U. Zywietz, A. B. Evlyukhin, C. Reinhardt, B. N. Chichkov, *Nat. Commun.* **2014**, *5*, 3402.
[55] S. Makarov, L. Kolotova, S. Starikov, U. Zywietz, B. Chichkov, *Nanoscale* **2018**, *10*, 11403.
[56] U. Zywietz, C. Reinhardt, A. B. Evlyukhin, T. Birr, B. N. Chichkov, *Appl. Phys. A* **2014**, *114*, 45.
[57] P. Dmitriev, S. Makarov, V. Milichko, I. Mukhin, A. Gudovskikh, A. Sitnikova, A. Samusev, A. Krasnok, P. Belov, *Nanoscale* **2016**, *8*, 5043.
[58] D. M. Zhigunov, D. A. Shilkin, N. G. Kokareva, V. O. Bessonov, S. A. Dyakov, D. A. Chermoshentsev, A. A. Mkrtchyan, Y. G. Gladush, A. A. Fedyanin, A. G. Nasibulin, *Nanotechnology* **2020**, *32*, 095206.
[59] J. H. Parker, D. W. Feldman, M. Ashkin, *Phys. Rev.* **1967**, *155*, 712.
[60] R. Kumar, M. Tanwar, *J. Raman Spectrosc.* **2021**, *52*, 2100.
[61] S. Veprek, F. A. Sarott, Z. Iqbal, *Phys. Rev. B* **1987**, *36*, 3344.
[62] V. S. Waman, M. M. Kamble, S. S. Ghosh, R. R. Hawaldar, D. P. Amalnerkar, V. G. Sathe, S. W. Gosavi, S. R. Jadkar, *Mater. Res. Bull.* **2012**, *47*, 3445.

[63] D. V. Tsu, B. S. Chao, S. R. Ovshinsky, S. J. Jones, J. Yang, S. Guha, R. Tsu, *Phys. Rev. B* **2001**, *63*, 125338.
[64] S. Q. Xiao, S. Xu, D. Y. Wei, S. Y. Huang, H. P. Zhou, Y. Xu, *J. Appl. Phys.* **2010**, *108*, 113520.
[65] D. M. Zhigunov, G. N. Kamaev, P. K. Kashkarov, V. A. Volodin, *Appl. Phys. Lett.* **2018**, *113*, 023101.
[66] J. E. Smith, M. H. Brodsky, B. L. Crowder, M. I. Nathan, A. Pinczuk, *Phys. Rev. Lett.* **1971**, *26*, 642.
[67] R. Kumar, G. Sahu, S. K. Saxena, H. M. Rai, P. R. Sagdeo, *Silicon* **2014**, *6*, 117.
[68] M. K. Kroychuk, A. S. Shorokhov, D. F. Yagudin, D. A. Shilkin, D. A. Smirnova, I. Volkovskaya, M. R. Shcherbakov, G. Shvets, A. A. Fedyanin, *Nano Lett.* **2020**, *20*, 3471.
[69] R. Alaee, C. Rockstuhl, I. Fernandez-Corbaton, *Opt. Commun.* **2018**, *407*, 17.
[70] A. B. Evlyukhin, C. Reinhardt, E. Evlyukhin, B. N. Chichkov, *J. Opt. Soc. Am. B* **2013**, *30*, 2589.
[71] A. B. Evlyukhin, B. N. Chichkov, *Phys. Rev. B* **2019**, *100*, 125415.

